Lidar-Based Safe Site Relative Navigation

Kari C. Ward*, Kyle W. Smith†
The Charles Stark Draper Laboratory

Isaac S. Rowe‡
Aerodyne Industries - Jacobs JETS II Contract

Jeanette M. Harper§
Odyssey Space Research

Davis W. Adams¶, Samuel M. Pedrotty‖, and Gavin F. Mendeck**
NASA Johnson Space Center

There has been a renewed focus in exploration of the lunar surface and maximizing scientific potential of such missions is made possible in part by minimizing the time required to set up operations; that is, reducing transit time on the surface by increasing the landing precision with respect to the intended target. Established Safe and Precise Landing–Integrated Capability Evolution (SPLICE) project precision landing requirements necessitate a navigation filter architecture and underlying models developed specifically with these needs in mind. To date, test flights to characterize SPLICE guidance and navigation (GN) system performance have not provided a means to divert from the *a priori* selected landing site (LS) due to hazardous conditions. With the inclusion of a new sensor, the hazard detection lidar (HDL), coupled with safe landing site selection algorithms, GN can divert from the originally planned trajectory and navigate relative to the new targeted landing site. This work presents a novel hazard relative measurement model and covariance transformation methodology that enable the navigation system to inform a safe-site relative guidance profile to meet project precision landing goals.

I. Background

As mission requirements tighten to meet specific project needs and advance the state-of-the-art, it is prudent to adapt the navigation filter to the mission design. In the context of planetary entry, descent, and landing (EDL), successful precision navigation is possible through incorporation of traditional and non-traditional information sources. New technologies have produced a wide array of non-traditional measurement sources by combining algorithms and sensors to extract information. To leverage these new technologies, modifications are made to the filter architecture itself, such as the use of multiple filters in parallel or target-relative estimation. These concepts are integral to some modern navigation systems such as that of the Orion program [1, 2].

The Safe and Precise Landing–Integrated Capability Evolution (SPLICE) project is also heavily invested in advancing EDL guidance and navigation (GN) capabilities [3]. Demonstrations and continued development of SPLICE project technologies are made possible through suborbital terrestrial test flights [4, 5] with the eventual goal of integration into missions to the moon and beyond. This discussion is concerned with the navigation filter design necessary to achieve the SPLICE program landing goals and requirements. To meet these targets, the SPLICE navigation filter is aided by several emergent technologies. Two unconventional systems are leveraged to ensure a safe and precise landing: a scanning hazard detection lidar, and a suite of site-targeter algorithms. These advanced systems are responsible for scanning and mapping the terrain surrounding the original intended landing site using the hazard detection lidar (HDL), evaluating that map for potential hazards, and selecting a new, safe landing site (site-targeter (ST)) to divert the vehicle. Ref. [6] presents a detailed discussion of these technologies.

*Senior Member Technical Staff
†Senior Member Technical Staff
‡GN&C Software Engineer
§Engineer
¶Navigation Engineer
‖Chief Engineer
**SPLICE PM

A divert from the planned trajectory occurs in the event that the original selected site is dangerous or more hazardous than previously understood and another site is identified to be safer through a combination of HDL and site-targeter analysis. Evaluation of the targeted landing site (LS) and candidates for a divert site are selected from an HDL-derived digital elevation map (DEM). Using a scanning lidar, the HDL fuses the resulting set of range measurements to provide an understanding of the local topography. The HDL provides a set of altitudes relative to a DEM origin point to construct the DEM at a fixed ground-sample distance. Additionally, an associated altitude uncertainty quantification is provided at each point.

SPLICE program requirements mandate that the GN system provide horizontal position knowledge with respect to the landing site within a relatively tight tolerance at the time of terminal descent initiation. There are several possible options for a target-aware filter design provided in literature, both inertial and relative [7]. Recently, a site-relative filter design was proposed that hinges on pointing the HDL boresight at the intended landing site - processing repeated scans of the terrain surrounding the LS to provide precise site relative knowledge even when the absolute knowledge of the LS may be poor [8]. Another design, a dual-inertial filter, was proposed and flight-tested in the Autonomous Landing and Hazard Avoidance Technologies (ALHAT) program. The ALHAT filter estimates the vehicle position, velocity, and attitude (PVA) in an inertial coordinate system and uses terrain scans to track known surface feature locations, and subsequently improve the map-tie error corrupting the landing site position estimate. The proposed design detailed here retains the inertially referenced vehicle PVA states in lieu of a fully relative filter, but instead estimates the LS position with respect to a planet-centered planet-fixed (PCPF) reference frame.

The changes to the SPLICE navigation filter fall under two categories: incorporation of the LS position estimate in the state vector, and novel DEM-based error models for performing the covariance reset. The latter of these changes are designed in such a way as to provide precision knowledge of the vehicle position relative to the intended divert landing site while retaining the stability of the existing inertially referenced filter that has successful flight heritage. The remainder of this discussion details the proposed architecture changes, relative to the current filter design, and processes for initialization and updates to the new estimated states to perform a landing site divert.

A. Acronyms

ALHAT Autonomous Landing and Hazard Avoidance Technologies
DEM digital elevation map
DQG dual quaternion guidance
EDL entry, descent, and landing
EKF extended Kalman filter
ENU east-north-up
GN guidance and navigation
HDL hazard detection lidar
HD hazard detection
IMU inertial measurement unit
JSC Johnson Space Center
LS landing site
LVLH local vertical local horizontal
MC Monte Carlo
MET mission ellapsed time
NDL navigation doppler lidar
PCPF planet-centered planet-fixed
PDI powered descent insertion
PVA position, velocity, and attitude
sMRP scaled modified Rodriguez parameter
SPLICE Safe and Precise Landing–Integrated Capability Evolution
TRN terrain relative navigation
ST site-targeter

B. Mathematical Notation

Throughout this discussion, $\circ$ is used to represent an arbitrary variable or quantity of appropriate size and definition, given the surrounding context.

1. Scalars, vectors, and matrices

- Scalar quantities are denoted with a non-bold symbol, e.g. a.
- Vectors quantities are denoted with a bold lower case symbol, e.g. $\boldsymbol{x}$
  - the length of a vector is given by $n_\circ$
  - $\tilde{\circ}$ denotes a unit vector
  - $\hat{\circ}$ denotes an estimated state or other random variable
  - Position vectors are given by $\boldsymbol{r}^c_{a/b}$ denoting the position of a with respect to point b, expressed in the c frame. Velocity vectors $\boldsymbol{v}^c_{a/b}$ follow the same notation. If, $b \triangleq c$, the point reference notation is not explicitly given, e.g. $\boldsymbol{r}^c_a$
- Matrices are given by bolder upper case symbols, e.g. $\boldsymbol{M}$
  - $\mathbf{0}_{n,m}$ is an n by m matrix of zeros, simplified as $\mathbf{0}_n$ if $n == m$
  - $\boldsymbol{I}_n$ is the square identity matrix of dimension n
  - $\mathrm{diag}(\circ)$ denotes a diagonal matrix comprised of the elements of vector $\circ$

2. Attitude

- Attitude states are parameterized by scalar first right-handed quaternions $\bar{\boldsymbol{q}}$, with estimate $\hat{\bar{\boldsymbol{q}}}$
- $\hat{\bar{\boldsymbol{q}}}^b_a = [\hat{q}^b_a \;\; \hat{\boldsymbol{q}}^b_a]^T$ gives the estimated quaternion for the transformation from frame a to b
- Attitude errors are parameterized by the scaled modified Rodriguez parameter (sMRP) $\Delta\phi$
- Quaternion multiplication is written such that $\bar{\boldsymbol{q}}^c_a = \bar{\boldsymbol{q}}^b_a \otimes \bar{\boldsymbol{q}}^c_b$
- The transformation matrix from frame c to d is given by $\boldsymbol{T}^d_c$

3. Operators and functions

- Superscript $\circ^T$ denotes the matrix or vector transpose
- Superscript $\circ^{-1}$ denotes the matrix or quaternion inverse (i.e conjugate)
- $|| \circ ||$ is the L_2 norm
- $[\circ\times]$ denotes the skew-symmetric cross product matrix for the vector $\circ$

4. Statistical quantities

- $\mathbb{E}\{\circ\}$ is the expected value function
- The standard deviation of a random variable is denoted by by $\sigma_\circ$
- $\boldsymbol{P}_{\boldsymbol{a},\boldsymbol{b}}$ is the cross-covariance matrix for arbitrary vectors $\boldsymbol{a}$ and $\boldsymbol{b}$
- *a priori* and *a posteriori* estimates are differentiated by $\circ^-$ and $\circ^+$, respectively

II. Planetary Navigation System Overview

The SPLICE navigation filter is responsible for estimating the vehicle PVA states throughout the flight. In addition to these primary states, the filter also estimates a collection of sensor biases and misalignments, and other quantities of interest.

A. Reference Frames

To describe these estimated states and process the suite of measurements available, several reference frames are necessary. General definitions and relevant details are as follows.

1. Inertial

- An inertial frame with origin at the center of the planet
- Denoted i

- Used as a common reference between other frames

2. *Fixed*
   - A planet-centered planet-fixed (PCPF) frame with the same origin as the inertial frame
   - Denoted f
   - Used in defining several terrain-aware measurement types
   - z-axis defined by the planet's mean axis of rotation

3. *DEM Local vertical local horizontal (LVLH)*
   - The reference frame for communication of HDL DEM data
   - A surface-fixed frame with origin at the LS
   - Denoted ℓ
   - Taken as 'quasi-inertial,' i.e. no rotational effects considered in the instantaneous definition of the frame
   - z-axis defined by the inertial vehicle position vector
   - y-axis defined by the vehicle inertial angular momentum vector
   - x-axis completes the right-handed triad, defines the along-track direction

4. *East-north-up (ENU)*
   - A surface-fixed frame with origin at the LS
   - Denoted enu
   - Rotates with the primary body
   - x, y, and z-axes in the local east, north, and up directions

5. *Inertial measurement unit (IMU)*
   - Navigation IMU-centered case frame
   - Denoted IMU
   - Principal vehicle reference frame through which all other vehicle-centered frames are related

6. *Sensors*
   - Sensor-specific reference frame centered on the sensor
   - Unique to each physical sensor
   - Measurement types from dual-functionality sensors (eg NDL: range and velocimetry) share a common sensor frame definition
   - Orientation and location defined relative to the IMU frame

B. Estimated states

The primary PVA states estimated by the filter are the IMU position $\hat{\boldsymbol{r}}^i_{IMU}$, velocity $\hat{\boldsymbol{v}}^i_{IMU}$, and attitude $\hat{\bar{\boldsymbol{q}}}^{IMU}_i$ with respect to the inertial frame. In addition to the estimated state vector, the filter also maintains a state error covariance estimate $\boldsymbol{P}_{\boldsymbol{x},\boldsymbol{x}}$. Due to the unit norm constraint of the quaternion, attitude error estimates are parameterized by sMRPs ϕ. Assuming small-angles, IMU attitude errors are denoted $\Delta\hat{\boldsymbol{\phi}}^{IMU}_i$, with the random variable itself given by $\hat{\boldsymbol{\phi}}^{IMU}_i$. The corresponding error quaternion is defined such that

$$\Delta\hat{\bar{\boldsymbol{q}}}^{IMU}_i = \begin{bmatrix} \frac{16-\Delta\hat{\boldsymbol{\phi}}^{IMU,T}_i\Delta\hat{\boldsymbol{\phi}}^{IMU}_i}{16+\Delta\hat{\boldsymbol{\phi}}^{IMU,T}_i\Delta\hat{\boldsymbol{\phi}}^{IMU}_i} \\ \frac{8\Delta\hat{\boldsymbol{\phi}}^{IMU}_i}{16+\Delta\hat{\boldsymbol{\phi}}^{IMU,T}_i\Delta\hat{\boldsymbol{\phi}}^{IMU}_i} \end{bmatrix} \tag{1}$$

The error quaternion in Eq. (1) can also be defined from

$$\Delta\hat{\bar{\boldsymbol{q}}}^{IMU}_i = \bar{\boldsymbol{q}}^{IMU}_i \otimes \hat{\bar{\boldsymbol{q}}}^{IMU,-1}_i\,, \tag{2}$$

and equivalently,

$$\boldsymbol{T}^i_{IMU} = \hat{\boldsymbol{T}}^i_{IMU} \left(\boldsymbol{I}_3 + \left[\Delta \hat{\boldsymbol{\phi}}^{IMU}_i \times \right] \right) . \tag{3}$$

Note, this dual parameterization of a reference attitude $\hat{\bar{\boldsymbol{q}}}^{IMU}_i$ and corresponding attitude error $\hat{\boldsymbol{\phi}}^{IMU}_i$ means the covariance dimension is one less than that of the estimated state vector.

The navigation filter is provided information through a suite of different sensors. State propagation is done by discrete dead reckoning of IMU gyroscope and accelerometer data. External state information is provided by a navigation doppler lidar (NDL), image-based terrain relative navigation (TRN), and a scanning HDL sensor. Each of these sensors has an associated set of corruptions (e.g. bias, misalignment, scale factor) that can be estimated by the filter. Collectively, these bias terms are denoted as $\hat{\boldsymbol{b}}_s$ for simplicity.

C. Filter States and Covariance

To facilitate precision landing capabilities, the PCPF frame position of the targeted landing site $\hat{\boldsymbol{r}}^f_{LS}$ is incorporated in the filter's estimated state vector. Maintaining a globally referenced estimate of the landing site position that is informed by precise HDL measurements allows for the vehicle-relative landing site position to be maintained with similarly high precision—even if the underlying globally referenced position vectors have much higher associated uncertainties.

The full filter estimated state is

$$\hat{\boldsymbol{x}} = \begin{bmatrix} \hat{\boldsymbol{r}}^i_{IMU} \\ \hat{\boldsymbol{v}}^i_{IMU} \\ \hat{\bar{\boldsymbol{q}}}^{IMU}_i \\ \hat{\boldsymbol{b}}_s \\ \hat{\boldsymbol{r}}^f_{LS} \end{bmatrix} \tag{4}$$

where again $\hat{\boldsymbol{b}}_s$ is a vector collection of sensor-specific biases and other corruptions given in the individual sensor frames. The corresponding covariance is then

$$\boldsymbol{P}_{\boldsymbol{x},\boldsymbol{x}} = \begin{bmatrix} \boldsymbol{P}_{\hat{\boldsymbol{r}}^i_{IMU},\hat{\boldsymbol{r}}^i_{IMU}} & \boldsymbol{P}_{\hat{\boldsymbol{r}}^i_{IMU},\hat{\boldsymbol{v}}^i_{IMU}} & \boldsymbol{P}_{\hat{\boldsymbol{r}}^i_{IMU},\hat{\boldsymbol{\phi}}^{IMU}_i} & \boldsymbol{P}_{\hat{\boldsymbol{r}}^i_{IMU},\hat{\boldsymbol{b}}_s} & \boldsymbol{P}_{\hat{\boldsymbol{r}}^i_{IMU},\hat{\boldsymbol{r}}^f_{LS}} \\ \boldsymbol{P}_{\hat{\boldsymbol{v}}^i_{IMU},\hat{\boldsymbol{r}}^i_{IMU}} & \boldsymbol{P}_{\hat{\boldsymbol{v}}^i_{IMU},\hat{\boldsymbol{v}}^i_{IMU}} & \boldsymbol{P}_{\hat{\boldsymbol{v}}^i_{IMU},\hat{\boldsymbol{\phi}}^{IMU}_i} & \boldsymbol{P}_{\hat{\boldsymbol{v}}^i_{IMU},\hat{\boldsymbol{b}}_s} & \boldsymbol{P}_{\hat{\boldsymbol{v}}^i_{IMU},\hat{\boldsymbol{r}}^f_{LS}} \\ \boldsymbol{P}_{\hat{\boldsymbol{\phi}}^{IMU}_i,\hat{\boldsymbol{r}}^i_{IMU}} & \boldsymbol{P}_{\hat{\boldsymbol{\phi}}^{IMU}_i,\hat{\boldsymbol{v}}^i_{IMU}} & \boldsymbol{P}_{\hat{\boldsymbol{\phi}}^{IMU}_i,\hat{\boldsymbol{\phi}}^{IMU}_i} & \boldsymbol{P}_{\hat{\boldsymbol{\phi}}^{IMU}_i,\hat{\boldsymbol{b}}_s} & \boldsymbol{P}_{\hat{\boldsymbol{\phi}}^{IMU}_i,\hat{\boldsymbol{r}}^f_{LS}} \\ \boldsymbol{P}_{\hat{\boldsymbol{b}}_s,\hat{\boldsymbol{r}}^i_{IMU}} & \boldsymbol{P}_{\hat{\boldsymbol{b}}_s,\hat{\boldsymbol{v}}^i_{IMU}} & \boldsymbol{P}_{\hat{\boldsymbol{b}}_s,\hat{\boldsymbol{\phi}}^{IMU}_i} & \boldsymbol{P}_{\hat{\boldsymbol{b}}_s,\hat{\boldsymbol{b}}_s} & \boldsymbol{P}_{\hat{\boldsymbol{b}}_s,\hat{\boldsymbol{r}}^f_{LS}} \\ \boldsymbol{P}_{\hat{\boldsymbol{r}}^f_{LS},\hat{\boldsymbol{r}}^i_{IMU}} & \boldsymbol{P}_{\hat{\boldsymbol{r}}^f_{LS},\hat{\boldsymbol{v}}^i_{IMU}} & \boldsymbol{P}_{\hat{\boldsymbol{r}}^f_{LS},\hat{\boldsymbol{\phi}}^{IMU}_i} & \boldsymbol{P}_{\hat{\boldsymbol{r}}^f_{LS},\hat{\boldsymbol{b}}_s} & \boldsymbol{P}_{\hat{\boldsymbol{r}}^f_{LS},\hat{\boldsymbol{r}}^f_{LS}} \end{bmatrix} , \tag{5}$$

where it should be noted that the dimension of the covariance matrix is $(n_{\boldsymbol{x}} - 1) \times (n_{\boldsymbol{x}} - 1)$ due to the disparate parameterization of attitude and attitude errors. The landing site related covariances $\boldsymbol{P}_{\hat{\boldsymbol{r}}^f_{LS},\hat{\circ}}$ are initialized as

$$\boldsymbol{P}_{\hat{\boldsymbol{r}}^f_{LS},\hat{\circ}} = \begin{cases} \sigma^2_{\hat{r}^f_{LS}} \boldsymbol{I}_3, & \text{if } \hat{\circ} \triangleq \hat{\boldsymbol{r}}^f_{LS} \\ \boldsymbol{0}_{3,n_{\hat{\circ}}}, & \text{otherwise} \end{cases} \tag{6}$$

where $\sigma_{\hat{r}^f_{LS}}$ is an *a priori* determined value for the original targeted landing site. The filter itself does not operate on the full covariance matrix given in Eq. (5), but instead uses a UD covariance factorization [9]. For simplicity, all developments in this discussion are detailed using a full covariance matrix, however any special considerations to accommodate the UD factorization in implementation will be noted.

D. Relative State Covariances

Although the position and velocity of the vehicle relative to the landing site are not estimated states in the state vector of Eq. (4), the filter's ability to intrinsically estimate these values is a primary focus of this work. Computation of the relative position is covered in the following section; however, the process for determining the relative covariances can be detailed using the definition of the covariance in Eq. (5). The landing site relative position covariance is defined as,

$$\boldsymbol{P}_{\hat{\boldsymbol{r}}^{enu}_{IMU/LS},\hat{\boldsymbol{r}}^{enu}_{IMU/LS}} = \boldsymbol{T}^{enu}_{f}\left(\boldsymbol{T}^{f}_{i}\boldsymbol{P}_{\hat{\boldsymbol{r}}^{i}_{IMU},\hat{\boldsymbol{r}}^{i}_{IMU}}\boldsymbol{T}^{i}_{f} + \boldsymbol{P}_{\hat{\boldsymbol{r}}^{f}_{LS},\hat{\boldsymbol{r}}^{f}_{LS}} - 2\left(\boldsymbol{T}^{f}_{i}\boldsymbol{P}_{\hat{\boldsymbol{r}}^{i}_{IMU},\hat{\boldsymbol{r}}^{f}_{LS}}\right)\right)\boldsymbol{T}^{f}_{enu} \tag{7}$$

and the relative velocity is given by

$$\begin{aligned}\boldsymbol{P}_{\hat{\boldsymbol{v}}^{enu}_{IMU/LS},\hat{\boldsymbol{v}}^{enu}_{IMU/LS}} = \boldsymbol{T}^{enu}_{f}\Big(&\boldsymbol{T}^{f}_{i}\boldsymbol{P}_{\hat{\boldsymbol{v}}^{i}_{IMU},\hat{\boldsymbol{v}}^{i}_{IMU}}\boldsymbol{T}^{i}_{f} - \left[\omega^{f}_{f/i}\times\right]\boldsymbol{P}_{\hat{\boldsymbol{r}}^{f}_{LS},\hat{\boldsymbol{r}}^{f}_{LS}}\left[\omega^{f}_{f/i}\times\right] \\ &- \left[\omega^{f}_{f/i}\times\right]\boldsymbol{P}_{\hat{\boldsymbol{r}}^{f}_{LS},\hat{\boldsymbol{v}}^{i}_{IMU}}\boldsymbol{T}^{i}_{f} + \boldsymbol{T}^{f}_{i}\boldsymbol{P}_{\hat{\boldsymbol{v}}^{i}_{IMU},\hat{\boldsymbol{r}}^{f}_{LS}}\left[\omega^{f}_{f/i}\times\right]\Big)\boldsymbol{T}^{f}_{enu}\end{aligned} \tag{8}$$

E. State and covariance update

Incorporation of the information provided by the external sensor suite is done through the extended Kalman filter (EKF) update. To facilitate later discussions, the general EKF update process is detailed here for an arbitrary measurement.

At the time associated with a received measurement $\boldsymbol{z}$, an expected measurement $\hat{\boldsymbol{z}}$ is computed using the *a priori* state estimate $\boldsymbol{x}^-$ at the time of the measurement, and the appropriate filter measurement model. An associated Jacobian $\boldsymbol{H}$ with dimension $n_{\boldsymbol{z}} \times (n_{\boldsymbol{x}} - 1)$ is computed by linearizing the measurement model about the *a priori* state estimate. The $n_{\boldsymbol{z}} \times n_{\boldsymbol{z}}$ dimension measurement noise covariance $\boldsymbol{R}$, *a priori* covariance $\boldsymbol{P}_{\boldsymbol{x},\boldsymbol{x}}$, and Jacobian are used to compute the residual covariance $\boldsymbol{W}$, cross-covariance $\boldsymbol{C}$, Kalman gain $\boldsymbol{K}$, and resulting updates via

$$\boldsymbol{W} = \boldsymbol{H}\boldsymbol{P}^-_{\boldsymbol{x},\boldsymbol{x}}\boldsymbol{H}^T + \boldsymbol{R} \tag{9a}$$

$$\boldsymbol{C} = \boldsymbol{P}^-_{\boldsymbol{x},\boldsymbol{x}}\boldsymbol{H}^T \tag{9b}$$

$$\boldsymbol{K} = \boldsymbol{C}\boldsymbol{W}^{-1} \tag{9c}$$

$$\boldsymbol{P}^+_{\boldsymbol{x},\boldsymbol{x}} = \left(\boldsymbol{I}_{(n_{\boldsymbol{x}}-1)} - \boldsymbol{K}\boldsymbol{H}\right)\boldsymbol{P}^-_{\boldsymbol{x},\boldsymbol{x}}\left(\boldsymbol{I}_{(n_{\boldsymbol{x}}-1)} - \boldsymbol{K}\boldsymbol{H}\right)^T + \boldsymbol{K}\boldsymbol{R}\boldsymbol{K}^T \tag{9d}$$

$$\Delta\boldsymbol{x} = \boldsymbol{K}(z - \hat{z}) \tag{9e}$$

$$\boldsymbol{x}^+ = \boldsymbol{x}^- + \Delta\boldsymbol{x} \tag{9f}$$

where it should be noted that the state update in Eq. (9f) is valid for all non-attitude states. For a given attitude error $\Delta\hat{\boldsymbol{\phi}}^{IMU}_i \in \Delta\boldsymbol{x}$, the *a posteriori* attitude estimate is given by

$$\hat{\bar{\boldsymbol{q}}}^{IMU,+}_i = \Delta\hat{\bar{\boldsymbol{q}}}^{IMU}_i \otimes \hat{\bar{\boldsymbol{q}}}^{IMU,-}_i \tag{10}$$

where $\Delta\hat{\bar{\boldsymbol{q}}}^{IMU}_i$ is given as a function of $\Delta\hat{\boldsymbol{\phi}}^{IMU}_i$ in Eq. (1).

III. HDL Measurement Processing

The information gained via the HDL scanning capabilities, opens up new opportunities for more precise site targeting and landing. However, the accuracy of the resulting HDL data products, as well as the performance of onboard guidance and control subsystems, are inherently tied to the precision and accuracy of the navigation filter's estimated state.

A. The DEM and Metadata

Observability of the LS position state is provided through HDL scans of the surrounding terrain. These scans are processed by the HDL and the resulting DEM is provided to the filter; that is, a set of altitudes on a fixed sized grid totaling 100m by 100m. The grid is defined by the LVLH frame of the vehicle at the start of the scan, centered at the DEM origin. This origin point is defined by the HDL boresight surface intersection point at the start of the HDL scan. The altitude values are provided relative to that of the DEM LVLH frame origin, which is taken to be 0, and each is accompanied by an associated standard deviation σ_{DEM} of the altitude values binned at each grid location. The DEM origin is used both as the aforementioned altitude reference, and to locate the DEM relative to the vehicle.

Upon creation, it is assumed the HDL DEM scan is subsequently provided to hazard detection (HD) and ST applications. These algorithms respectively evaluate the scan for potential hazards, and provide a set of candidate safe landing sites. The particulars of the HD and ST applications are not the focus of this work; as a result, the filter is assumed to receive the highest scoring (i.e. safest) divert site from ST when it receives the corresponding DEM scan.

B. The Estimated Divert Landing Site and Error Sources

Upon receiving a DEM and a new divert site location from ST, the covariance components related to the landing site position can be reset to reflect the underlying relationship between the vehicle PVA states and the landing site location estimate. This is accomplished such that information about the vehicle-relative LS position is preserved in the cross-covariance values after the reset is performed. First, the LS position is defined in the PCPF reference frame from multiple pieces of information provided with the scan data as

$$\hat{\boldsymbol{r}}^{f}_{LS} = \boldsymbol{T}^{f}_{i}\left(\hat{\boldsymbol{r}}^{i}_{IMU} + \hat{\boldsymbol{T}}^{i}_{IMU}\boldsymbol{r}^{IMU}_{DEM_0} + \hat{\boldsymbol{T}}^{i}_{\ell}\boldsymbol{r}^{\ell}_{LS/DEM_0}\right) \tag{11}$$

where $\boldsymbol{r}^{IMU}_{DEM_0}$ is the location of the DEM origin reference point relative the the IMU, in the IMU case frame, provided as part of the DEM scan meta data, and $\boldsymbol{r}^{\ell}_{LS/DEM_0}$ is the divert site location relative to the DEM origin, in the LVLH frame, provided by ST. The PCPF frame referenced landing site defined in Eq. (11) is taken as truth and replaces the filter's LS state estimate. The geometry of the problem defined in Eq. (11) is depicted in Figure (1) for a lunar descent scenario. The HDL DEM is shown in orange with a pink grid of points. The inertial position of the vehicle IMU (grey) is used to provide an absolute reference when combined with the relative position of the DEM with respect to the IMU (green) and the divert site location relative to the DEM center (orange). The resulting PCPF frame landing site location (purple star) is the estimated state in the navigation filter. The objective of the divert procedure established in the following subsections is to define the uncertainties associated with the vectors depicted in Figure (1) such that the uncertainty in the position of the landing site relative to the vehicle (blue) remains small.

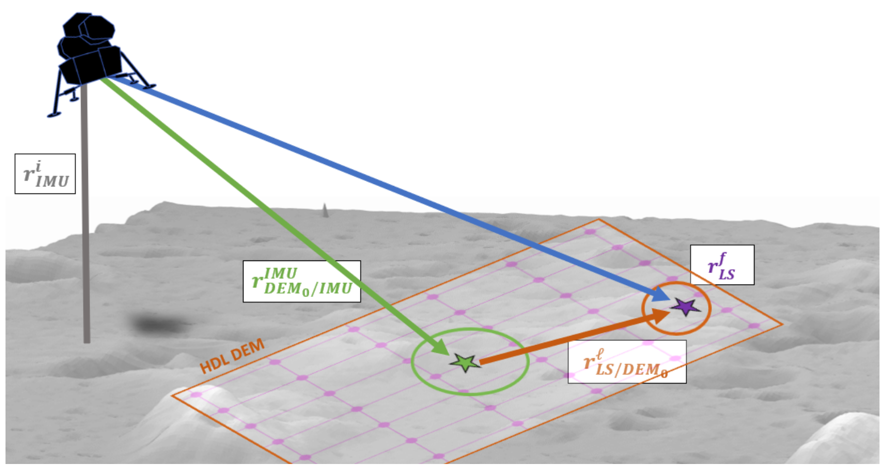

Fig. 1 Geometry of Eq. (11) for establishing the divert landing site location in PCPF using the DEM meta data

Leveraging Eq. (11), it is of interest to define sources of errors in the relative vectors that define the new landing site, depicted by the orange and green circles in Figure (1). These vectors, $\boldsymbol{r}^{IMU}_{DEM_0}$ and $\boldsymbol{r}^{\ell}_{LS/DEM_0}$ are subject to errors in the filter's estimated PVA states and errors stemming from the underlying HDL measurements. The divert LS in Eq. (11) can be equivalently defined as

$$\hat{\boldsymbol{r}}^{f}_{LS} = \boldsymbol{T}^{f}_{i}\left(\hat{\boldsymbol{r}}^{i}_{IMU} + \hat{\boldsymbol{T}}^{i}_{IMU}\left(\boldsymbol{r}^{IMU}_{HDL} + \rho\hat{\boldsymbol{T}}^{IMU}_{HDL}\tilde{\boldsymbol{r}}^{HDL}_{DEM_0}\right) + \hat{\boldsymbol{T}}^{i}_{\ell}\boldsymbol{r}^{\ell}_{LS/DEM_0}\right) \tag{12}$$

where $\boldsymbol{r}^{IMU}_{HDL}$ is the position of the HDL sensor relative to the IMU, given in the IMU case frame, ρ is the range from the HDL to the DEM origin, and $\tilde{\boldsymbol{r}}^{HDL}_{DEM_0}$ is the unit vector for the position of the DEM origin relative to the HDL. The change in formulation of the LS definition for Eq. (12) to use HDL-relative, as opposed to the IMU-relative DEM origin vector in Eq. (11), allows for the consideration of errors in $\hat{\boldsymbol{T}}^{IMU}_{HDL}$ due to HDL sensor misalignment, as detailed in Section (III.B.3).

Inspection of Eq. (12) again shows two primary components, similar to Eq. (11), that go into the definition of $\hat{\boldsymbol{r}}^{f}_{LS}$, the PCPF location of the center of the DEM, that is

$$\hat{\boldsymbol{r}}^{f}_{DEM_0} = \boldsymbol{T}^{f}_{i}\left(\hat{\boldsymbol{r}}^{i}_{IMU} + \hat{\boldsymbol{T}}^{i}_{IMU}\left(\boldsymbol{r}^{IMU}_{HDL} + \rho\hat{\boldsymbol{T}}^{IMU}_{HDL}\tilde{\boldsymbol{r}}^{HDL}_{DEM_0}\right)\right) \tag{13}$$

and the LVLH-frame relative vector from the DEM origin to the selected divert site, transformed into the PCPF frame, given by

$$\hat{\boldsymbol{r}}^{f}_{LS/DEM_0} = \boldsymbol{T}^{f}_{i}\hat{\boldsymbol{T}}^{i}_{\ell}\boldsymbol{r}^{\ell}_{LS/DEM_0} . \tag{14}$$

Equations (13) and (14) provide a convenient separation of terms to define sensitivities of $\hat{\boldsymbol{r}}^{f}_{LS}$ with respect to the other estimated states in Eq. (4).

1. Range Error Model

The first three terms in Eq. (12), also given in Eq. (13) for the PCPF location of the DEM origin, follow a slant-range measurement model with easily defined sensitivities with respect to the vehicle inertial position and attitude states. To first order, the range model sensitivities of the PCPF LS position vector due to vehicle position and attitude estimate errors are given by

$$\boldsymbol{H}^{\rho}_{\hat{\boldsymbol{r}}^{i}_{IMU}} = \boldsymbol{T}^{f}_{i} , \tag{15}$$

for the position and

$$\boldsymbol{H}^{\rho}_{\hat{\boldsymbol{\phi}}^{IMU}_{i}} = -\boldsymbol{T}^{f}_{i}\hat{\boldsymbol{T}}^{i}_{IMU}\left[\boldsymbol{r}^{IMU}_{HDL}\times\right] - \rho\left(\boldsymbol{T}^{f}_{i}\hat{\boldsymbol{T}}^{i}_{IMU}\left[\tilde{\boldsymbol{r}}^{HDL}_{HDL/DEM_0}\times\right]\right) , \tag{16}$$

for the attitude, where $\circ^{\rho}$ denotes that these sensitivities are related to the range error model. Equations (15) and (16) provide a linear mapping describing how position and attitude errors contribute to errors in the new divert site position estimate.

2. LVLH Error Model

The last term in Eq. (12), also given in Eq. (14), defines the PCPF-frame position of the divert landing site, relative to the DEM center. While none of the estimated states in Eq. (4) appear directly in Eq. (14), the vehicle inertial position and velocity are used to define the LVLH frame at the time of the scan. The LVLH frame origin is placed at the DEM origin point and the frame definition is chosen so that the LVLH frame rotates with the primary body, tying the LVLH frame to the estimated state (and associated uncertainty) at the scan start time. The LVLH frame is defined by the down-range $\tilde{\boldsymbol{a}}_{\ell}$, cross-range $\tilde{\boldsymbol{c}}_{\ell}$, and altitude $\tilde{\boldsymbol{h}}_{\ell}$ directions, for the given position and velocity.

The LVLH frame basis vectors expressed in the inertial frame define a transformation $\hat{\boldsymbol{T}}^{\ell}_{i}$ from inertial to LVLH as

$$\boldsymbol{T}^{\ell}_{i} = \left[\tilde{\boldsymbol{a}}^{i}_{\ell}\ \ \tilde{\boldsymbol{c}}^{i}_{\ell}\ \ \tilde{\boldsymbol{h}}^{i}_{\ell}\right]^{T} . \tag{17}$$

The transformation matrix and basis vectors in Eq. (17) are defined from the estimated states expressed in the inertial frame as

$$\tilde{\boldsymbol{h}}^{i}_{\ell} = \frac{\hat{\boldsymbol{r}}^{i}_{IMU}}{||\hat{\boldsymbol{r}}^{i}_{IMU}||} \tag{18a}$$

$$\boldsymbol{c}^{i}_{\ell} = \hat{\boldsymbol{r}}^{i}_{IMU} \times \hat{\boldsymbol{v}}^{i}_{IMU} \tag{18b}$$

$$\tilde{\boldsymbol{c}}^{i}_{\ell} = \frac{\boldsymbol{c}^{i}_{\ell}}{||\boldsymbol{c}^{i}_{\ell}||} \tag{18c}$$

$$\boldsymbol{a}^{i}_{\ell} = \boldsymbol{c}^{i}_{\ell} \times \hat{\boldsymbol{r}}^{i}_{IMU} \tag{18d}$$

$$\tilde{\boldsymbol{a}}^{i}_{\ell} = \frac{\boldsymbol{a}^{i}_{\ell}}{||\boldsymbol{a}^{i}_{\ell}||} . \tag{18e}$$

The definition of the inertial to LVLH transformation in Eq. (17) and its use in Eq. (12) allows for the modeling of sensitivities in the landing site position estimate to transformation errors caused by the estimated vehicle position and velocity error at the start of the scan. Defining this relationship can be done through partials of the transformation basis vectors in Eqs. (18a), (18c), and (18e) with respect to the filter states, that is

$$\frac{\partial \hat{\boldsymbol{T}}_i^\ell}{\partial \hat{\boldsymbol{r}}^i_{IMU}} = \begin{bmatrix} \frac{\partial \hat{\boldsymbol{T}}_i^\ell}{\partial \hat{r}^i_{(1),IMU}} \\ \frac{\partial \hat{\boldsymbol{T}}_i^\ell}{\partial \hat{r}^i_{(2),IMU}} \\ \frac{\partial \hat{\boldsymbol{T}}_i^\ell}{\partial \hat{r}^i_{(3),IMU}} \end{bmatrix} \tag{19}$$

$$\frac{\partial \hat{\boldsymbol{T}}_i^\ell}{\partial \hat{\boldsymbol{v}}^i_{IMU}} = \begin{bmatrix} \frac{\partial \hat{\boldsymbol{T}}_i^\ell}{\partial \hat{v}^i_{(1),IMU}} \\ \frac{\partial \hat{\boldsymbol{T}}_i^\ell}{\partial \hat{v}^i_{(2),IMU}} \\ \frac{\partial \hat{\boldsymbol{T}}_i^\ell}{\partial \hat{v}^i_{(3),IMU}} \end{bmatrix} \tag{20}$$

where $\hat{\circ}_{(i)}$ denotes the ith component of the vector $\hat{\circ}$. Using the matrix derivative chain rule approach of [10] and a similar derivation of LVLH frame sensitivities to that of [11], the mappings for the vehicle position and velocity errors to errors in the relative LS position of Eq. (14) are

$$\boldsymbol{H}^\ell_{\hat{r}^i_{IMU}} = \boldsymbol{T}_i^f \begin{bmatrix} \boldsymbol{r}^{i,T}_{LS/DEM_0} \frac{\partial \tilde{\boldsymbol{a}}^i_\ell}{\partial \hat{\boldsymbol{r}}^i_{IMU}} \\ \boldsymbol{r}^{i,T}_{LS/DEM_0} \frac{\partial \tilde{\boldsymbol{c}}^i_\ell}{\partial \hat{\boldsymbol{r}}^i_{IMU}} \\ \boldsymbol{r}^{i,T}_{LS/DEM_0} \frac{\partial \tilde{\boldsymbol{h}}^i_\ell}{\partial \hat{\boldsymbol{r}}^i_{IMU}} \end{bmatrix}, \tag{21}$$

for the position, and

$$\boldsymbol{H}^\ell_{\hat{v}^i_{IMU}} = \boldsymbol{T}_i^f \begin{bmatrix} \boldsymbol{r}^{i,T}_{LS/DEM_0} \frac{\partial \tilde{\boldsymbol{a}}^i_\ell}{\partial \hat{\boldsymbol{v}}^i_{IMU}} \\ \boldsymbol{r}^{i,T}_{LS/DEM_0} \frac{\partial \tilde{\boldsymbol{c}}^i_\ell}{\partial \hat{\boldsymbol{v}}^i_{IMU}} \\ \boldsymbol{r}^{i,T}_{LS/DEM_0} \frac{\partial \tilde{\boldsymbol{h}}^i_\ell}{\partial \hat{\boldsymbol{v}}^i_{IMU}} \end{bmatrix}, \tag{22}$$

for the velocity. The partials in Eqs. (21) and (22), for the LVLH frame basis vectors with respect to the inertial vehicle position and velocity, are defined as

$$\frac{\partial \tilde{\boldsymbol{h}}^i_\ell}{\partial \hat{\boldsymbol{r}}^i_{IMU}} = \frac{\partial \hat{\tilde{\boldsymbol{r}}}^i_{IMU}}{\partial \hat{\boldsymbol{r}}^i_{IMU}} = \frac{\boldsymbol{I}_3 - \hat{\tilde{\boldsymbol{r}}}^i_{IMU} \hat{\tilde{\boldsymbol{r}}}^{i,T}_{IMU}}{||\hat{\boldsymbol{r}}^i_{IMU}||} \tag{23}$$

$$\frac{\partial \tilde{\boldsymbol{h}}^i_\ell}{\partial \hat{\boldsymbol{v}}^i_{IMU}} = \boldsymbol{0}_{3,3} \tag{24}$$

$$\frac{\partial \tilde{\boldsymbol{c}}^i_\ell}{\partial \hat{\boldsymbol{r}}^i_{IMU}} = \frac{\partial \tilde{\boldsymbol{c}}^i_\ell}{\partial \boldsymbol{c}^i_\ell} \frac{\partial \boldsymbol{c}^i_\ell}{\partial \hat{\boldsymbol{r}}^i_{IMU}} = -\left(\frac{\boldsymbol{I}_3 - \tilde{\boldsymbol{c}}^i_\ell \tilde{\boldsymbol{c}}^{i,T}_\ell}{||\boldsymbol{c}^i_\ell||}\right) \left[\hat{\boldsymbol{v}}^i_{IMU} \times\right] \tag{25}$$

$$\frac{\partial \tilde{\boldsymbol{c}}^i_\ell}{\partial \hat{\boldsymbol{v}}^i_{IMU}} = \frac{\partial \tilde{\boldsymbol{c}}^i_\ell}{\partial \boldsymbol{c}^i_\ell} \frac{\partial \boldsymbol{c}^i_\ell}{\partial \hat{\boldsymbol{v}}^i_{IMU}} = \left(\frac{\boldsymbol{I}_3 - \tilde{\boldsymbol{c}}^i_\ell \tilde{\boldsymbol{c}}^{i,T}_\ell}{||\boldsymbol{c}^i_\ell||}\right) \left[\hat{\boldsymbol{r}}^i_{IMU} \times\right] \tag{26}$$

$$\frac{\partial \tilde{\boldsymbol{a}}^i_\ell}{\partial \hat{\boldsymbol{r}}^i_{IMU}} = \frac{\partial \tilde{\boldsymbol{a}}^i_\ell}{\partial \boldsymbol{a}^i_\ell} \frac{\partial \boldsymbol{a}^i_\ell}{\partial \hat{\boldsymbol{r}}^i_{IMU}} = \left(\frac{\boldsymbol{I}_3 - \tilde{\boldsymbol{a}}^i_\ell \tilde{\boldsymbol{a}}^{i,T}_\ell}{||\boldsymbol{a}^i_\ell||}\right) \left(- \left[\boldsymbol{h}^i_\ell \times\right] \frac{\partial \boldsymbol{c}^i_\ell}{\partial \hat{\boldsymbol{r}}^i_{IMU}} - \left[\boldsymbol{c}^i_\ell \times\right] \frac{\partial \boldsymbol{h}^i_\ell}{\partial \hat{\boldsymbol{r}}^i_{IMU}}\right) \tag{27}$$

$$= \left(\frac{\boldsymbol{I}_3 - \tilde{\boldsymbol{a}}^i_\ell \tilde{\boldsymbol{a}}^{i,T}_\ell}{||\boldsymbol{a}^i_\ell||}\right) \left(\left[\boldsymbol{h}^i_\ell \times\right] \left[\hat{\boldsymbol{v}}^i_{IMU} \times\right] + \left[\boldsymbol{c}^i_\ell \times\right]\right) \tag{28}$$

$$\frac{\partial \tilde{\boldsymbol{a}}^i_\ell}{\partial \hat{\boldsymbol{v}}^i_{IMU}} = \frac{\partial \tilde{\boldsymbol{a}}^i_\ell}{\partial \boldsymbol{a}^i_\ell} \frac{\partial \boldsymbol{a}^i_\ell}{\partial \hat{\boldsymbol{v}}^i_{IMU}} = \left(\frac{\boldsymbol{I}_3 - \tilde{\boldsymbol{a}}^i_\ell \tilde{\boldsymbol{a}}^{i,T}_\ell}{||\boldsymbol{a}^i_\ell||}\right) \left(- \left[\boldsymbol{h}^i_\ell \times\right] \frac{\partial \boldsymbol{c}^i_\ell}{\partial \hat{\boldsymbol{v}}^i_{IMU}} - \left[\boldsymbol{c}^i_\ell \times\right] \frac{\partial \boldsymbol{h}^i_\ell}{\partial \hat{\boldsymbol{v}}^i_{IMU}}\right) \tag{29}$$

$$= -\left(\frac{\boldsymbol{I}_3 - \tilde{\boldsymbol{a}}^i_\ell \tilde{\boldsymbol{a}}^{i,T}_\ell}{||\boldsymbol{a}^i_\ell||}\right) \left[\boldsymbol{h}^i_\ell \times\right] \left[\hat{\boldsymbol{r}}^i_{IMU} \times\right] \tag{30}$$

3. Other Error Sources

Although the HDL sensor misalignment $\hat{\boldsymbol{\phi}}^{IMU}_{HDL}$ is not an estimated state in the filter, the effects of uncertainty in the sensor mounting can be considered in the LS position covariance reset, provided the alignment error covariance can be quantified. This covariance $\boldsymbol{P}_{\hat{\boldsymbol{\phi}}^{IMU}_{HDL},\hat{\boldsymbol{\phi}}^{IMU}_{HDL}}$ is taken to be uncorrelated and small enough to adhere to the small-angle assumption. The sensitivities of the LS position in Eq. (12) to the HDL misalignment are, to first order, given by

$$\boldsymbol{H}_{\hat{\boldsymbol{\phi}}^{IMU}_{HDL}} = -\rho \boldsymbol{T}^f_i \hat{\boldsymbol{T}}^i_{IMU} \hat{\boldsymbol{T}}^{IMU}_{HDL} \left[\tilde{\boldsymbol{r}}^{HDL}_{HDL/DEM_0} \times\right] \tag{31}$$

The last two remaining noise sources incorporated in the covariance reset are the DEM-reported altitude uncertainty at the divert location σ^2_{DEM} and tuning noise applied in the along-track σ_a, cross-track σ_c, and altitude σ_h directions of the LVLH frame. These tuning noises capture other unmodeled errors induced through the DEM creation process.

The DEM-reported altitude uncertainty, tuning noise, and HDL misalignment uncertainty are collected for convenience into a single sensor noise covariance

$$\boldsymbol{R}_{HDL} = \boldsymbol{H}_{\hat{\boldsymbol{\phi}}^{IMU}_{HDL}} \boldsymbol{P}_{\hat{\boldsymbol{\phi}}^{IMU}_{HDL},\hat{\boldsymbol{\phi}}^{IMU}_{HDL}} \boldsymbol{H}^T_{\hat{\boldsymbol{\phi}}^{IMU}_{HDL}} + \hat{\boldsymbol{T}}^f_\ell \begin{bmatrix} \sigma^2_a & 0 & 0 \\ 0 & \sigma^2_c & 0 \\ 0 & 0 & \sigma^2_h + \sigma^2_{DEM} \end{bmatrix} \hat{\boldsymbol{T}}^{f,T}_\ell \tag{32}$$

C. Divert Landing Site Covariance Reset

Resetting the $\hat{\boldsymbol{r}}^f_{LS}$ covariance components to reflect the uncertainties associated with the new estimated landing site location can be handled in several different ways. The chosen reset follows the "zero-time propagation" approach of [8], with some modifications to accommodate the SPLICE filter's UD covariance factorization.

1. Full Covariance Approach

The reset approach can be conceptualized as mapping the covariance in Eq. (5) from the original state space defined by the vector in Eq. (4) with the original landing site, to a new state space that is otherwise identical, except with $\hat{\boldsymbol{r}}^f_{LS}$ estimating the new divert landing site. The mapping $\boldsymbol{H}^*$ from the old state space to the new state space is therefore defined as identity for all non-LS related terms, and otherwise serves to collect and apply the estimated-state-dependent sensitivities defined in Sections (III.B.1) and (III.B.2) such that the LS-related uncertainties and cross-correlations are appropriately established.

Using the covariance definition in Eq. (5), the range and LVLH model sensitivities in Eqs. (15) and (21) for position, the LVLH model sensitivity in Eq. (22) for velocity, and range model sensitivity in Eq. (16) for attitude, the mapping is defined as

$$\boldsymbol{H}^* = \begin{bmatrix} \boldsymbol{I}_3 & \boldsymbol{0}_3 & \boldsymbol{0}_3 & \boldsymbol{0}_{3,n_{\hat{b}_s}} & \boldsymbol{0}_3 \\ \boldsymbol{0}_3 & \boldsymbol{I}_3 & \boldsymbol{0}_3 & \boldsymbol{0}_{3,n_{\hat{b}_s}} & \boldsymbol{0}_3 \\ \boldsymbol{0}_3 & \boldsymbol{0}_3 & \boldsymbol{I}_3 & \boldsymbol{0}_{3,n_{\hat{b}_s}} & \boldsymbol{0}_3 \\ \boldsymbol{0}_{n_{\hat{b}_s},3} & \boldsymbol{0}_{n_{\hat{b}_s},3} & \boldsymbol{0}_{n_{\hat{b}_s},3} & \boldsymbol{I}_{n_{\hat{b}_s},n_{\hat{b}_s}} & \boldsymbol{0}_{n_{\hat{b}_s},3} \\ \left(\boldsymbol{H}^\rho_{\hat{\boldsymbol{r}}^i_{IMU}} + \boldsymbol{H}^\ell_{\hat{\boldsymbol{r}}^i_{IMU}}\right) & \boldsymbol{H}^\ell_{\hat{\boldsymbol{v}}^i_{IMU}} & \boldsymbol{H}^\rho_{\hat{\boldsymbol{\phi}}^{IMU}_i} & \boldsymbol{0}_{3,n_{\hat{b}_s}} & \boldsymbol{0}_3 \end{bmatrix}. \tag{33}$$

The sensor-related uncertainties and tuning noises defined in Section (III.B.3), and collected in Eq. (32), must also be incorporated into the new landing site position covariance. Define an $[(n_{\boldsymbol{x}} - 1) \times (n_{\boldsymbol{x}} - 1)]$ matrix $\boldsymbol{R}^*$ such that

$$\boldsymbol{R}^* = \begin{bmatrix} \boldsymbol{0}_3 & \boldsymbol{0}_3 & \boldsymbol{0}_3 & \boldsymbol{0}_{3,n_{\hat{b}_s}} & \boldsymbol{0}_3 \\ \boldsymbol{0}_3 & \boldsymbol{0}_3 & \boldsymbol{0}_3 & \boldsymbol{0}_{3,n_{\hat{b}_s}} & \boldsymbol{0}_3 \\ \boldsymbol{0}_3 & \boldsymbol{0}_3 & \boldsymbol{0}_3 & \boldsymbol{0}_{3,n_{\hat{b}_s}} & \boldsymbol{0}_3 \\ \boldsymbol{0}_{n_{\hat{b}_s},3} & \boldsymbol{0}_{n_{\hat{b}_s},3} & \boldsymbol{0}_{n_{\hat{b}_s},3} & \boldsymbol{0}_{n_{\hat{b}_s},n_{\hat{b}_s}} & \boldsymbol{0}_{n_{\hat{b}_s},3} \\ \boldsymbol{0}_3 & \boldsymbol{0}_3 & \boldsymbol{0}_3 & \boldsymbol{0}_3 & \boldsymbol{R}_{HDL} \end{bmatrix}. \tag{34}$$

where $\boldsymbol{R}_{HDL}$ is given in Eq. (32). With the state covariance mapping defined in Eq. (33) and the external noise and sensor uncertainties in Eq. (34), the covariance reset is performed via

$$\boldsymbol{P}^*_{\boldsymbol{x},\boldsymbol{x}} = \boldsymbol{H}^*\boldsymbol{P}_{\boldsymbol{x},\boldsymbol{x}}\boldsymbol{H}^{*,T} + \boldsymbol{R}^* \tag{35}$$

where the resulting $\boldsymbol{P}^*_{\boldsymbol{x},\boldsymbol{x}}$ is identical to $\boldsymbol{P}_{\boldsymbol{x},\boldsymbol{x}}$, the covariance prior to the divert, except in the covariances and cross-covariance terms related to the landing site position estimate; that is, for the definition in Eq. (5), the last three rows. The covariance reset in Eq. (35) appropriately handles the collection of contributions of the vehicle position, velocity, and attitude uncertainties in the computation of the new landing site covariance through the mapping matrix defined in Eq. (33), along with incorporation of the external sensor and tuning noises through the noise matrix Eq. (34).

2. UD Factorized Approach

Section (III.C.1) establishes the reset procedure for a full covariance representation of the filter uncertainty; however, the SPLICE architecture uses a $\boldsymbol{UD}$ factorized approach to provide enhanced numerical stability. Instead of operating on the full covariance matrix defined in Eq. (5), the SPLICE filter uses an upper triangular matrix $\boldsymbol{U}$ with ones on the diagonal, and a diagonal matrix $\boldsymbol{D}$ such that

$$\boldsymbol{P}_{\boldsymbol{x},\boldsymbol{x}} = \boldsymbol{U}\boldsymbol{D}\boldsymbol{U}^T \, . \tag{36}$$

Implementing the $\boldsymbol{UD}$ factorized definition in Eq. (36), the full covariance reset of Eq. (35) can be written as

$$\boldsymbol{P}^*_{\boldsymbol{x},\boldsymbol{x}} = \boldsymbol{U}^*\boldsymbol{D}^*\boldsymbol{U}^{*,T} = \boldsymbol{H}^*\boldsymbol{U}\boldsymbol{D}\boldsymbol{U}^T\boldsymbol{H}^{*,T} + \boldsymbol{R}^* \, . \tag{37}$$

Computing the new post-divert $\boldsymbol{U}^*$ and $\boldsymbol{D}^*$ can be achieved using the procedure detailed in Ref. [12] for the time propagation of the $\boldsymbol{UD}$ factorized uncertainty from time $k-1$ to k; that is, a $\boldsymbol{UD}$ formulation for the "zero-time propagation" reset method of Ref. [8].

Following Ref. [12], define matrices

$$\boldsymbol{Y} = [\boldsymbol{H}^*\boldsymbol{U} \quad \boldsymbol{G}^*] \tag{38}$$

$$\boldsymbol{Q} = \begin{bmatrix} \boldsymbol{D} & \boldsymbol{0}_{\boldsymbol{x}} \\ \boldsymbol{0}_{\boldsymbol{x}} & \boldsymbol{I}_{\boldsymbol{x}} \end{bmatrix} \tag{39}$$

where $\boldsymbol{G}^*$ is the *lower* triangular Cholesky factor of $\boldsymbol{R}^*$. Modified Gram-Schmidt Orthogonalization is then used, along with the matrix definitions of Eqs. (38) and (39), to compute the basis vectors of a matrix $\boldsymbol{T} = [\boldsymbol{T}_1 \quad \boldsymbol{T}_2]$ such that the desired $\boldsymbol{U}^*$ and $\boldsymbol{D}^*$ can be found via

$$\boldsymbol{Y}\boldsymbol{T}^{-T} = [\boldsymbol{U}^* \quad \boldsymbol{0}_{\boldsymbol{x}}] \tag{40}$$

and

$$\boldsymbol{D}^* = \boldsymbol{T}_1^T\boldsymbol{Q}\boldsymbol{T}_1 \, . \tag{41}$$

It should be noted that $\boldsymbol{G}^*$ in Eq. (38) and $\boldsymbol{I}_{\boldsymbol{x}}$ in Eq. (39) (where the process noise covariance would usually go) are used in combination to apply the noise matrix $\boldsymbol{R}^*$ in the reset procedure, while also adhering the diagonal assumption on $\boldsymbol{Q}$ in Ref. [12].

IV. Simulation

The new SPLICE navigation filter divert process is demonstrated in the closed-loop SPLICE lunar landing simulation. The scenario used in this analysis, depicted in Figure (2), starts just after the deorbit burn above the lunar north pole and runs to 30 meters above the lunar surface near the south pole. The simulation framework leverages NASA's Trick toolkit [13, 14] to provide job scheduling, data recording, and Monte Carlo (MC) capabilities. The SPLICE guidance and navigation software is simulated as a payload interfacing with a host vehicle that provides control outputs corresponding to the input guidance solution. The host vehicle dynamics are simulated using the Johnson Space Center (JSC) Engineering Orbital Dynamics package.

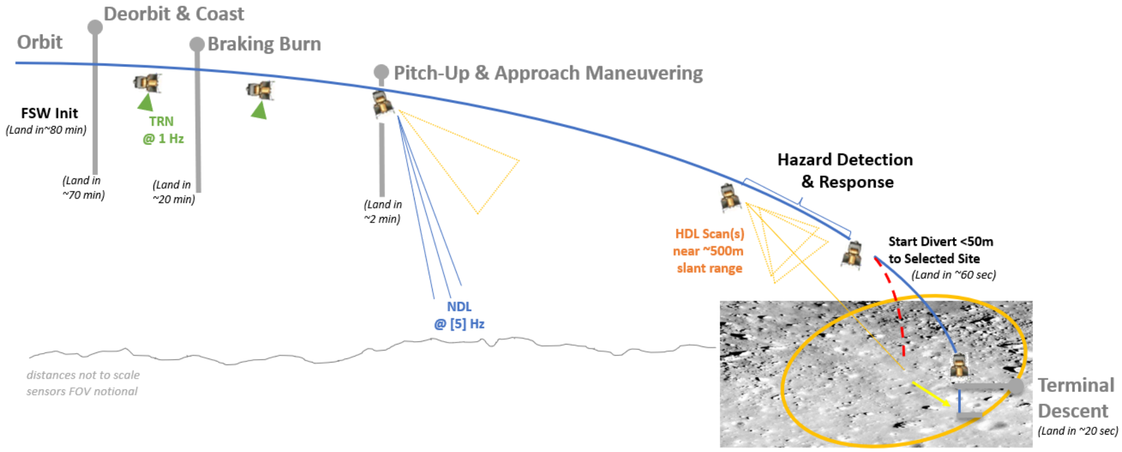

Fig. 2 The SPLICE concept of operations for the simulated lunar descent to landing with HDL scan and divert

The guidance algorithms used for the descent vary depending on the phase of flight. For the deorbit burn, coast, and powered descent insertion (PDI) burns a combination of an initial reference trajectory and tuneable Apollo guidance are leveraged. Prior to PDI the vehicle maintains a constant attitude with respect to the nadir lunar surface to maintain sensor pointing. After the PDI burn, SPLICE guidance takes over using dual quaternion guidance (DQG) [15, 16]. DQG performs path planning using the relative states with respect to the intended landing site that are computed from the filter's estimated states of inertial PVA of the IMU, and PCPF absolute landing site location.

The SPLICE navigation filter receives measurement data throughout the descent from several sources, in addition to the HDL DEM that is the focus of these developments. With the exception of the HDL, the sensor suite follows the configuration used in SPLICE's New Shepard test flights [5]. Simulated measurements of NDL range and velocity along with TRN pixel pairs and candidate feature locations comprise the external information, while the IMU measurements are used for propagation of the filter's time-varying state estimates. IMU accelerations and angular rates are available for the entire descent while TRN and NDL are active before and after the PDI burn, respectively.

Initial covariance values for the vehicle inertial PVA states are 33.33 m, 0.5 m/s, and 0.5 deg (1σ per-axis). The filter covariance is initialized as uncorrelated. For this configuration, the bias vector $\hat{\boldsymbol{b}}_s$ in Eq. (4) is comprised of IMU acceleration and angular rate biases, TRN focal length bias and sensor mounting misalignment, and NDL range and velocity biases (per beam, three beams total). Each of these corruptions has a corresponding corruption applied in the simulated measurements.

There are a handful of notable differences in the filter and simulation truth models. Most noticeable in this analysis is a difference in gyro statistics discussed in more detail in Section (V). The simulation models mass depletion due to thrusting events, while the filter does not. This causes motion in the center of gravity for the vehicle over the course of the descent that is not captured in the filter's static model. The filter uses a spherical gravity model for the moon, whereas the simulation truth model is given by the LP150Q with degree/order 8. The truth model also includes spherical models for Earth and Sun gravitational effects; the filter does not consider 3rd-body effects.

Development of the HDL to HD and ST pipeline and MC capabilities for the SPLICE simulations is an ongoing process. For this analysis HDL scan is simulated using a pre-computed DEM comprising a grid of elevations. Specifically, it is a synthetic DEM of the Apollo 12 landing site discussed in more detail in Ref. [6] and shown in Figure (3). After a fixed elapsed simulation time, the inertial vector to the center point of the DEM LVLH frame is computed from the current estimated HDL position and attitude via an ellipsoidal model of the range to the surface. This information is combined with the elevations and transformed into a format resembling a measurement packet from the HDL sensor. Placement of the true DEM location and divert site position in PCPF are computed in a similar fashion using the host vehicle states at the time of the scan. After the scan is completed, the HD and ST algorithm outputs are simulated using a predetermined set of safe sites depicted in Figure (3). For each MC run, one of the ten safe sites is randomly selected for the divert.

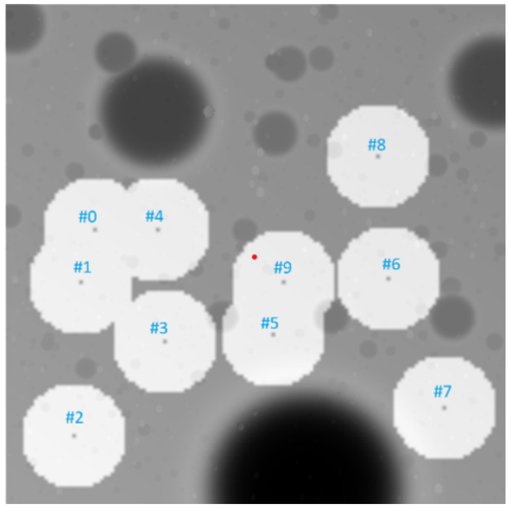

Fig. 3 Simulation DEM and set of divert site locations used in MC analysis. DEM LVLH frame origin is given by the red dot.

V. Results

Performance of the new navigation filter capability is examined with MC error statistics of 1000 runs for the simulation described in Section (IV). Results for these runs are given in Figures (4)–(11), depicting a combination of the single run filter error and corresponding uncertainty (given as $\pm 3\sigma$) as well as snapshots of the filter error at key points in the descent that have been identified as critical in the SPLICE concept of operations. For results with time as the independent variable, values are given relative to the HDL scan time of 4149 seconds mission ellapsed time (MET).

There are several events of note in the results: TRN begins collecting imagery at approximately -3400s, a pitchover and maneuver to prepare for the HDL scan at approximately -750s, NDL begins returning range and velocity measurements between -175s to -75s, and finally the HDL scan at 0s.

The first set of results, given in Figures (4)–(6) gives the inertial PVA state errors for each MC run and corresponding $\pm 3\sigma$. Although the relative state tracking is of particular interest to this work, the inertial frame IMU states are the primary estimates for the vehicle. A major trend shared by all three sets of inertial results is the large discrepancy between the MC error and the filter $\pm 3\sigma$ lines. The MC statistics are captured by the filter uncertainty with very little exception, but the filter leaves something to be desired in terms of precision. This is due to a mismatch in the filter's statistics for the IMU, specifically the gyro process noise covariance and bias uncertainty, and the corresponding values used for the truth. In accordance with the findings of Ref. [17], the filter statistics are inflated to 10x the truth values to compensate for unmodeled effects such as IMU misalignment, scale factor, and readout noise, in addition to unknown control errors and several known mismatches in modeling previously discussed in Section (IV). Since the advanced IMU models are still future work for simulation development, the filter appears overly cautious in the current comparison, especially until the final minutes of the descent, when controller errors and large rapid maneuvers are a primary driver of filter error.

The second set of results in Figures (7)–(8) gives the distribution of filter position and velocity errors in the inertial frame at HDL scan time and ENU east/north plane at terminal descent start. Due to the pole-to-pole descent trajectory, the inertial x-y plane and ENU east-north plane are approximately the LVLH cross-range/down-range plane. To ensure a quality HDL scan and selection of a divert site within the SPLICE GNC system capabilities, requirements are placed on the distribution of inertial state errors at the time of the scan. Results in Figure (7) show the velocity distribution (Figure (7b) blue dots) is well within the performance goal (red circle). The inertial position distribution in Figure (7a) appears to be within the goal, in terms of standard deviation, but also shows a bias in the results. Several of the aforementioned modeling mismatches between the filter and the simulation truth could be contributing to the position error bias, namely the center of gravity modeling, second order and third body gravitational effects, controller modeling errors, as well as potential timing offsets between truth and filter data logging. Further investigation is needed to determine the root cause, but the error spread suggests the filter is capable of meeting this performance goal once the bias is addressed.

Results in Figure (8) at the start of terminal descent (30m altitude) give the east-north plane position and velocity error distributions (blue dots) relative to the SPLICE performance goal. Velocity results in Figure (8b) are well within the target, while the position results in Figure (8a) show the only SPLICE project goal that the filter is truly struggling to meet in this analysis: the terminal descent position error distribution. While most of the runs are captured within the performance goal, a significant enough number are exceeding this threshold that position error performance is a key component of future work.

The last set of results are given in Figures (9)–(11) detailing the absolute landing site and landing site relative quantities of interest. The absolute landing site performance in Figure (9) gives the single run error and filter statistics for the landing site position in PCPF. There are two stark differences in these results compared to the other error with $\pm 3\sigma$ presented here, namely the zero error for all runs prior to the divert, and the growth in the filter uncertainty seen most prominently in the y-axis results (middle subplot). The former is due to the deterministic original landing site location - the filter is initialized with an arbitrary uncertainty in that state, but since no measurements are processed that provide observability for the state, there is no change in the filter estimate or covariance. The growth in the filter uncertainty at the time of the divert is due to the nature of the covariance reset. Since the reset in Eq. (35) is not a Kalman filter update, there is no guarantee of uncertainty reduction in the absolute state by this operation. It should also be noted that some single run errors in Figure (9) and Figures (10)–(11) exhibit a large jump that is rectified on the next time step. This is an artifact induced by data logging in simulation where the truth divert is processed after the filter and thus the change in intended landing site is not reflected in the truth data until the next major frame.

Relative covariances for position and velocity of the vehicle with respect to the landing site are computed via Eqs. (7) and (8). Site-relative position results in Figure (10) demonstrate the effectiveness of the covariance reset, wherein the filter snaps down to a much tighter 3σ interval after the divert is processed. The filter then maintains consistent-to-slightly-cautious estimation (i.e. the filter 3σ captures the MC error distribution with some wiggle-room) of the relative position until the terminal descent hand-off. Examination of the filter standard deviation behavior post-divert hints at the primary issue preventing the filter from meeting the relative position terminal descent performance goal in Figure (8a). That is, after the divert is processed, little-to-no convergence occurs in the inertial position uncertainty in Figure (4), the PCPF landing site position uncertainty in Figure (9), and consequently also the ENU relative position uncertainty in Figure (10). The only source of position state information post-scan is the NDL which is not specifically oriented to point at the landing site and does not provide sufficient state observability to allow the filter to converge further in any of the aforementioned position estimates. Relative velocity results in Figure (11) show the filter gains more information in this state through the maneuvers that occur prior to, and in response to, the divert. This is evidenced by the large spread of single run filter $\pm 3\sigma$ values where different guidance divert responses cause differing convergence and observability in the velocity.

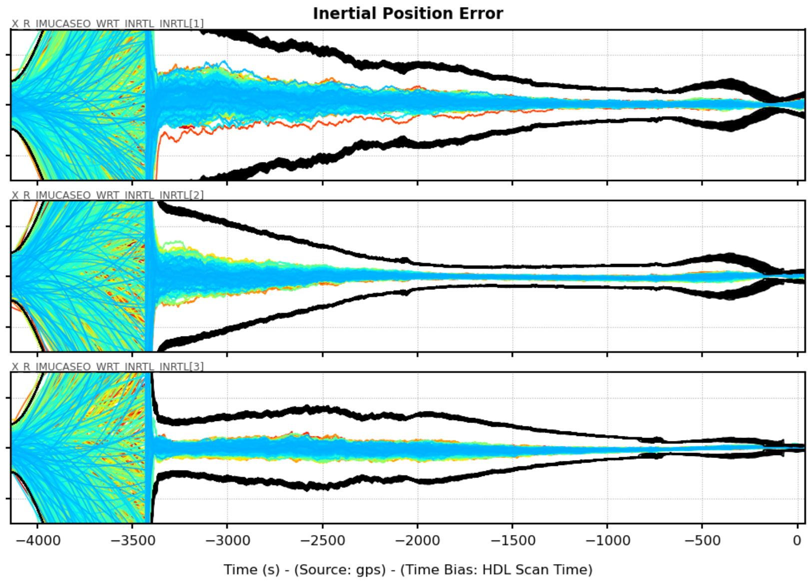

Fig. 4 MC error (colored lines) in the filter estimate of the inertial position of the IMU, with filter $\pm 3\sigma$ (black lines)

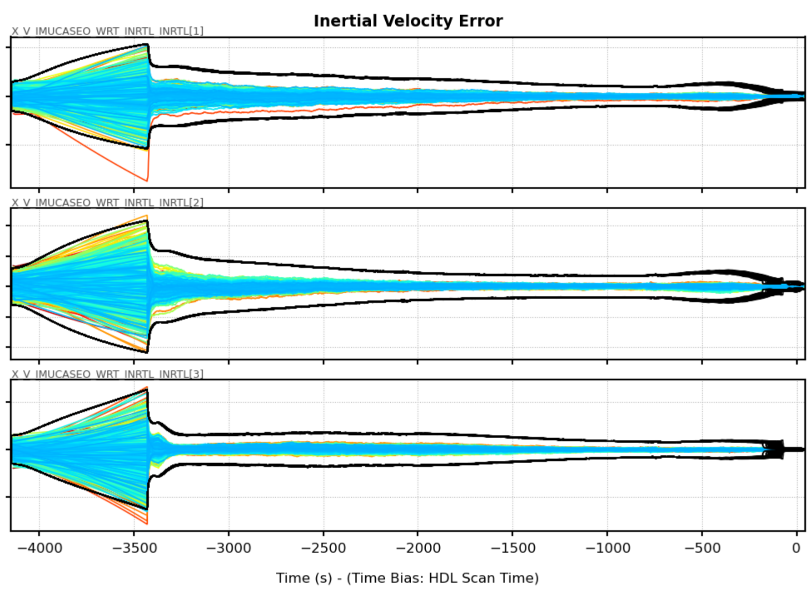

Fig. 5 MC error (colored lines) in the filter estimate of the inertial velocity of the IMU, with filter $\pm 3\sigma$ (black lines)

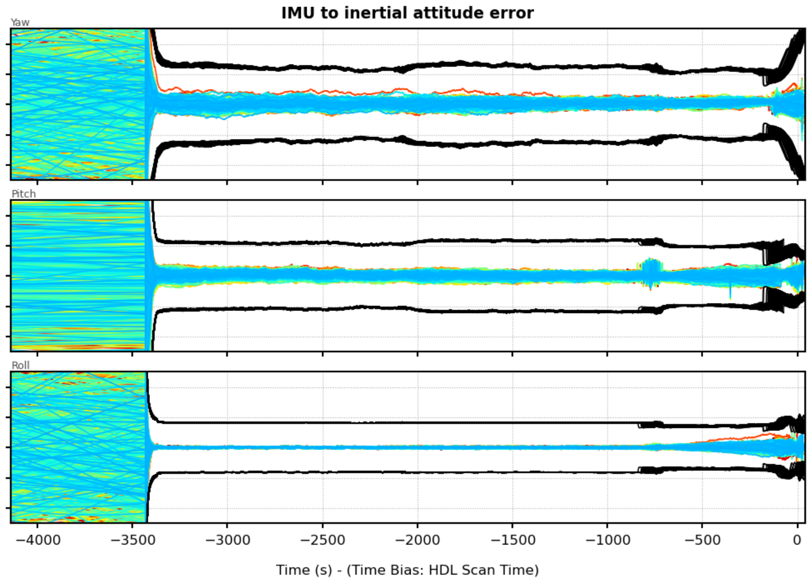

Fig. 6 MC error (colored lines) in the filter estimate of the IMU attitude with respect to inertial, with filter $\pm 3\sigma$ (black lines)

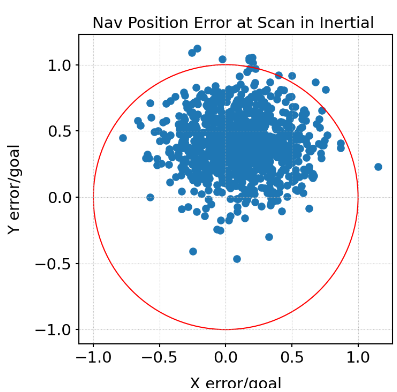

(a) MC position error distribution in inertial x-y plane (blue dots) with respect to the SPLICE performance goal (red circle) at HDL scan time

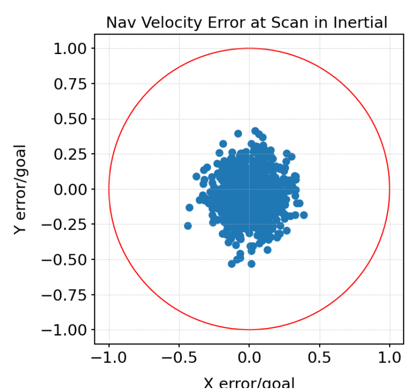

(b) MC velocity error distribution in inertial x-y plane (blue dots) with respect to the SPLICE performance goal (red circle) at HDL scan time

Fig. 7 Navigation errors at HDL scan time - relative to the SPLICE performance goals

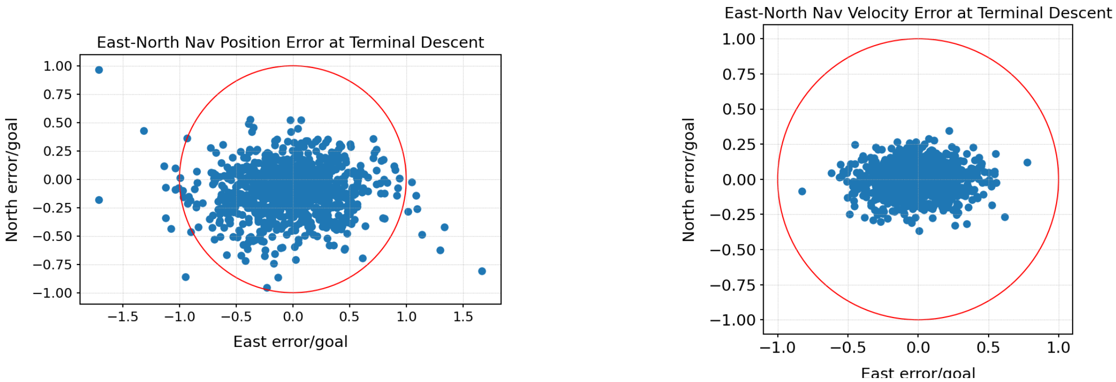

(a) MC position error distribution in east-north (blue dots) scaled to the SPLICE performance goal (red circle) at terminal descent

(b) MC velocity error distribution in east-north (blue dots) scaled to the SPLICE performance goal (red circle) at terminal descent

Fig. 8 Navigation errors at terminal descent - relative to the SPLICE performance goals

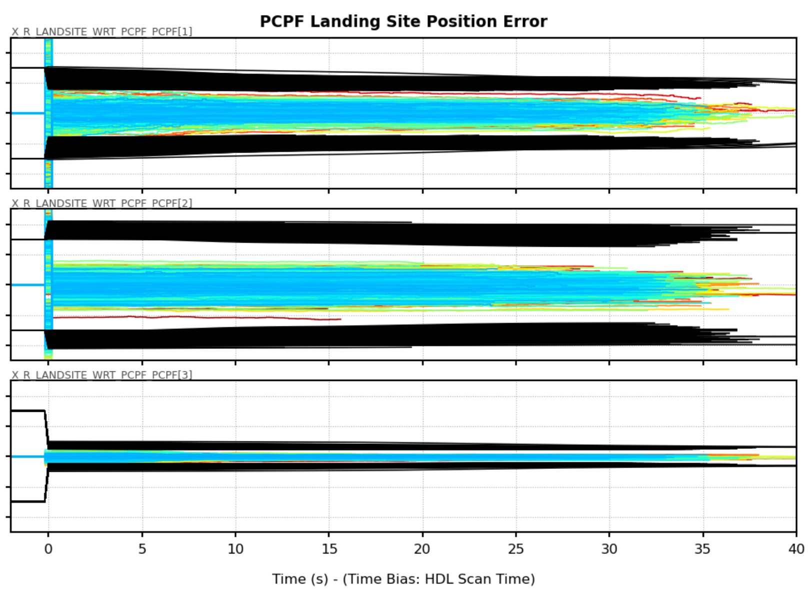

Fig. 9 MC error (colored lines) in absolute landing site location with respect to PCPF with filter $\pm 3\sigma$ (black lines)

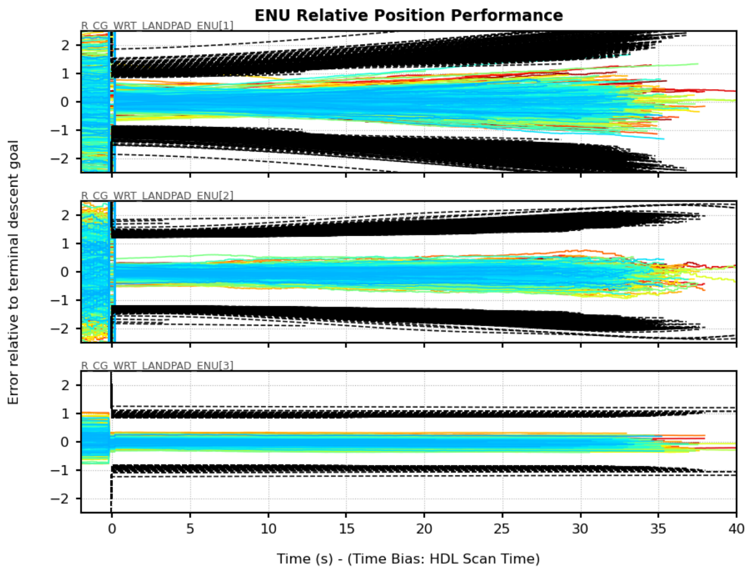

Fig. 10 Vehicle landing site-relative position MC error (colored lines) in the ENU frame with computed $\pm 3\sigma$ (black lines). Results scaled to the corresponding SPLICE terminal descent performance goal.

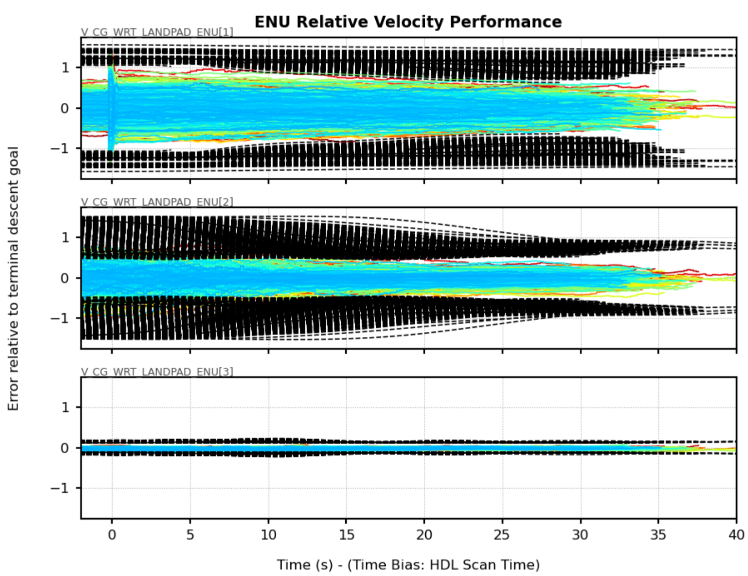

Fig. 11 Vehicle landing site-relative velocity MC error (colored lines) in the ENU frame with computed $\pm 3\sigma$ (black lines). Results scaled to the corresponding SPLICE terminal descent performance goal.

VI. Conclusions

This paper provides a summary of a safe site relative navigation approach that leverages HDL scans to inform a divert from the original landing site and a filter covariance reset design that emphasizes precise site-relative position knowledge. The SPLICE navigation filter has performed well in terrestrial test flight campaigns, but has not until recently been applied to a lunar landing scenario. In addition to pivoting to a lunar descent concept of operations, the SPLICE goals for navigation emphasize precise landing relative to a divert safe site selected from an HDL DEM scan of the surrounding terrain. To achieve these goals without upending the existing flight-heritage architecture, the filter estimates the absolute location of the landing site and incorporates specific correlations in the covariance designed such that precise relative position and velocity knowledge is maintained even in the presence of larger absolute state errors.

To test the navigation filter developments that are the focus of this work and other SPLICE algorithm research, the SPLICE simulation and flight software teams have built an ambitious and capable closed-loop framework that enables rapid guidance and navigation algorithm development and testing, with fidelity that would not be possible otherwise. Monte Carlo simulation results show the filter to be stable, but intentionally cautious in its estimation of the error statistics. The new divert covariance reset procedure provides relative state knowledge despite not directly estimating any relative states. Overall, the filter is demonstrably capable of meeting all but one of the SPLICE performance goals: the position error distribution at terminal descent.

There is not a simple straightforward path to achieving the SPLICE terminal descent performance goals given the current concept of operations. The only source of external information about the vehicle states leading up to terminal descent is in the form of NDL range and velocity measurements. While ranging is clearly sufficient to perform a safe landing, without further direct relative or absolute measurements of the targeted landing site, or other more informative measurement types, a precise landing is not yet guaranteed. New state information is crucial to supplement the NDL, without such, meeting program goals consistently will be challenging - but the SPLICE team has repeatedly shown they are capable of meeting lofty challenges.

Forward work to improve the navigation filter performance is focused on increasing the available state information post-HDL scan. While NDL range and velocity alone have been shown to be insufficient for meeting project goals, other available resources such as the DEM and terrain camera are promising avenues for improving performance through expanded imagery collection and data fusion.

Acknowledgments

The authors would like to thank Dr. Christopher D'Souza, Mr. Matthew Fritz, and Dr. Renato Zanetti for their invaluable time, feedback, and support in the development of this work. This work was authored by employees of Draper under Contract No. 80JSC021DA005 with the National Aeronautics and Space Administration.

References

[1] Holt, G. N., D'Souza, C. N., and Saley, D. W., "Orion Optical Navigation Progress Toward Exploration Mission 1," *Space Flight Mechanics Meeting*, Kissimmee, FL, 2018. https://doi.org/10.2514/6.2018-1978, URL https://arc.aiaa.org/doi/abs/10.2514/6.2018-1978.

[2] Woffinden, D., Zanetti, R., Tuggle, K., D'Souza, C., and Spehar, P., "Re-evaluating Orion's relative navigation filter design for NASA's future exploration missions," *Advances in the Astronautical Sciences AAS Guidance, Navigation, and Control Conference*, 2018.

[3] Sostaric, R. R., Pedrotty, S., Carson, J. M., Estes, J. N., Amzajerdian, F., Dwyer-Cianciolo, A. M., and Blair, J. B., "The SPLICE Project: Safe and Precise Landing Technology Development and Testing," *AIAA Scitech 2021 Forum*, 2021. https://doi.org/10.2514/6.2021-0256, URL https://arc.aiaa.org/doi/abs/10.2514/6.2021-0256.

[4] Smith, K., Olguin, A., Fritz, M., Lovelace, R., Sostaric, R. R., Pedrotty, S., Estes, J., Tse, T., and Garcia, R., "Operational Constraint Analysis of Terrain Relative Navigation for Landing Applications," *AIAA Scitech 2020 Forum*, 2020. https://doi.org/10.2514/6.2020-0370, URL https://arc.aiaa.org/doi/abs/10.2514/6.2020-0370.

[5] Fritz, M., Doll, J., Ward, K. C., Mendeck, G., Sostaric, R. R., Pedrotty, S., Kuhl, C., Acikmese, B., Bieniawski, S. R., Strohl, L., and Berning, A. W., "Post-Flight Performance Analysis of Navigation and Advanced Guidance Algorithms on a Terrestrial Suborbital Rocket Flight," *AIAA SCITECH 2022 Forum*, 2022. https://doi.org/10.2514/6.2022-0765, URL https://arc.aiaa.org/doi/abs/10.2514/6.2022-0765.

[6] Restrepo, C. I., Chen, P.-T., Sostaric, R. R., and Carson, J. M., "Next-Generation NASA Hazard Detection System Development," *AIAA Scitech 2020 Forum*, 2020. https://doi.org/10.2514/6.2020-0368.

[7] Woffinden, D., "Evaluating Relative Navigation Filter Designs and Architectures for Human Spaceflight," *Advances in the Astronautical Sciences AAS Guidance, Navigation, and Control Conference*, Vol. 172, 2020.

[8] Steffes, S. R., DeTrempe, P., Barton, G., and Woffinden, D., "Hazard Boresight Relative Navigation for Safe Lunar Landing," *AIAA SCITECH 2023 Forum*, 2023. https://doi.org/10.2514/6.2023-0691, URL https://arc.aiaa.org/doi/abs/10.2514/6.2023-0691.

[9] Bierman, G. J., *Factorization Methods for Discrete Sequential Estimation*, Dover Publications, New York, NY, 2006.

[10] Vetter, W., "Derivative operations on matrices," *IEEE Transactions on Automatic Control*, Vol. 15, No. 2, 1970, pp. 241–244. https://doi.org/10.1109/TAC.1970.1099409.

[11] Geller, D. K., Rose, M. B., and Woffinden, D. C., "Event Triggers in Linear Covariance Analysis with Applications to Orbital Rendezvous," *Journal of Guidance, Control, and Dynamics*, Vol. 32, No. 1, 2009, pp. 102–111. https://doi.org/10.2514/1.36834, URL https://doi.org/10.2514/1.36834.

[12] Carpenter, J. R., and D'Souza, C. N., "Navigation Filter Best Practices," Tech. Rep. TP–2018–219822, April 2018.

[13] Paddock, E., Lin, A., Vetter, K., and Crues, E., "Trick - A Simulation Development Toolkit," *AIAA Modeling and Simulation Technologies Conference and Exhibit*, 2003. https://doi.org/10.2514/6.2003-5809, URL https://arc.aiaa.org/doi/abs/10.2514/6.2003-5809.

[14] Penn, J., and Lin, A., "The Trick Simulation Toolkit: A NASA/Opensource Framework for Running Time Based Physics Models," *AIAA Modeling and Simulation Technologies Conference*, 2016. https://doi.org/10.2514/6.2016-1187, URL https://arc.aiaa.org/doi/abs/10.2514/6.2016-1187.

[15] Strohl, L., Doll, J., Fritz, M., Berning, A. W., White, S., Bieniawski, S. R., Carson, J. M., and Açikmeşe, B., "Implementation of a Six Degree of Freedom Precision Lunar Landing Algorithm Using Dual Quaternion Representation," *AIAA SCITECH 2022 Forum*, 2022. https://doi.org/10.2514/6.2022-1831, URL https://arc.aiaa.org/doi/abs/10.2514/6.2022-1831.

[16] Doll, J. A., Wagner, S. T., Fritz, M. P., Jang, J., Harper, J. M., Smith, K. W., Açikmeşe, B., Pedrotty, S. M., and Mendeck, G. F., "Performance Analysis of a Dual Quaternion Guidance Algorithm used during Lunar Approach with a Hazard Avoidance Maneuver," *2024 AIAA SciTech Conference*, 2024.

[17] DeMars, K. J., and Ward, K. C., "Modular framework for implementation and analysis of recursive filters with considered and neglected parameters," *NAVIGATION*, Vol. 67, No. 4, 2020, pp. 843–863. https://doi.org/https://doi.org/10.1002/navi.388.